

Log-periodic oscillations as real-time signatures of hierarchical dynamics in proteins

Emanuel Dorbath,¹ Adnan Gulzar,¹ and Gerhard Stock¹

Biomolecular Dynamics, Institute of Physics, University of Freiburg, 79104 Freiburg, Germany

(Dated: 21 November 2023)

The time-dependent relaxation of a dynamical system may exhibit a power-law behavior that is superimposed by log-periodic oscillations. Sornette [Phys. Rep. **297**, 239 (1998)] showed that this behavior can be explained by a discrete scale invariance of the system, which is associated with discrete and equidistant timescales on a logarithmic scale. Examples include such diverse fields as financial crashes, random diffusion, and quantum topological materials. Recent time-resolved experiments and molecular dynamics simulations suggest that discrete scale invariance may also apply to hierarchical dynamics in proteins, where several fast local conformational changes are a prerequisite for a slow global transition to occur. Employing entropy-based timescale analysis and Markov state modeling to a simple one-dimensional hierarchical model and biomolecular simulation data, it is found that hierarchical systems quite generally give rise to logarithmically spaced discrete timescales. By introducing a one-dimensional reaction coordinate that collectively accounts for the hierarchically coupled degrees of freedom, the free energy landscape exhibits a characteristic staircase shape with two metastable end states, which causes the log-periodic time evolution of the system. The period of the log-oscillations reflects the effective roughness of the energy landscape, and can in simple cases be interpreted in terms of the barriers of the staircase landscape.

I. INTRODUCTION

Complex systems such as biomolecules exhibit motions on many timescales, ranging from sub-picosecond vibrations to global conformational rearrangements requiring seconds.^{1,2} Rather than being uncoupled as assumed in normal mode theory,³ these molecular motions may interact in a nonlinear and cooperative manner, such that fast fluctuations are a prerequisite of rare transitions.^{4,5} The basic concept of such a hierarchical coupling of multiscala motions is often illustrated by a one-dimensional (1D) model of the free energy landscape, which represents the dynamics on different timescales by various tiers of the energy.^{6–9} As an example, Fig. 1a displays a free energy landscape showing three tiers A, B and C, which are associated with specific processes happening on μs , ns and ps timescales, respectively. Because the system needs to cross the barriers of tier C to reach the barriers of tier B and tier A, the hierarchical model give a simple explanation of the mechanistic coupling between fast and slow motions.

While the concept of a hierarchical energy landscape is appealing, the microscopic nature of the tiers and the associated couplings between them is not well understood. In principle, such mechanisms can be inferred directly from all-atom molecular dynamics (MD) simulations, which reveal the local structural changes that are required for a global conformational rearrangement.¹⁰ For example, by considering the left- to right-handed transitions of the helical peptide Aib₉, Buchenberg et al.⁵ showed that these global transitions (occurring on a $0.1\mu\text{s}$ timescale) first require conformational transitions of individual residues (which take about 1 ns), which in turn require the opening and closing of structure-stabilizing hydrogen bonds (occurring within tens of ps). Since the rates of these three processes were found to exhibit a

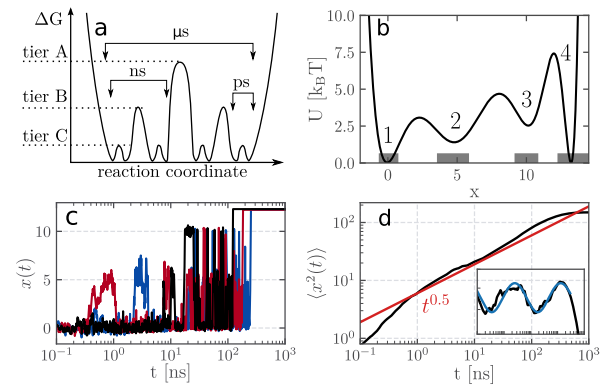


FIG. 1. Hierarchical dynamics in proteins. (a) Scheme of a hierarchical free energy landscape that represents dynamical processes on μs , ns and ps timescales by tiers A, B and C. (b) One-dimensional (1D) model potential $U(x)$, consisting of states 1–4 connected via energy barriers of similar height. Gray regions at the bottom define cores of the states used in Markov state modeling. (c) Time evolution $x(t)$ of three sample trajectories starting at $x = 0$, which need several attempts to gradually climb over consecutive energy barriers. (d) Averaging over many trajectories, the resulting mean squared displacement $\langle x^2(t) \rangle$, in black) shows a power-law behavior ($\propto t^{0.5}$, in red) that is superimposed by log-periodic oscillations. The enclosure shows a fit (blue) of the oscillatory residual $R(t)$ defined in Eq. (21).

similar temperature behavior, they concluded that the heights of the corresponding energy barriers must be similar, which appears to be in contrast to the energy landscape shown in Fig. 1a.

Represented by a one-dimensional (1D) model, these findings leads to a staircase-like energy landscape $U(x)$ depicted in Fig. 1b. The model consists of four states that are separated by three energy barriers, whose similar height ($\sim 3k_B T$) corresponds roughly to the energy required to break a hydrogen bond. In this way, x could be considered as collective coordinate constructed from the sum of three hydrogen bond distances.¹¹ Assuming that the system starts at time $t = 0$ in state **1**, it evolves via intermediate states **2** and **3**, and finally reaches the second low-energy state **4**. Figure 1c shows three sample trajectories $x(t)$ of the model, see Methods for details. Starting in state **1**, the system will initially cross the first barrier to state **2**, but then typically fall back to **1** due to the high back-rate of the model. After some attempts, a rare fluctuation may drive the system over the second barrier to reach state **3**, until after many more attempts the system will eventually reach the final state **4**. Using a logarithmic representation of time, this gradual climbing over similar energy barriers manifest itself in apparent log-oscillations of $x(t)$.

To explain these findings, we assume that the mean transition time over the first barrier (with energy E_b) is given by $\tau_{1 \rightarrow 2} = \tau_0 e^{-\beta E_b}$, where $\beta = 1/k_B T$ denotes the inverse temperature. Since all barriers are similar, we roughly estimate that transitions over the first two barriers take about $\tau_{1 \rightarrow 3} = \tau_0 e^{-2\beta E_b}$, and analogously $\tau_{1 \rightarrow 4} = \tau_0 e^{-3\beta E_b}$. This leads to the relation

$$\log \tau_{1 \rightarrow n+1} - \log \tau_{1 \rightarrow n} = \beta E_b \log e, \quad (1)$$

where $\log e = \log x / \ln x$ denotes the decadic logarithm of Euler's number. It states that the system exhibits discrete and equidistant timescales on a logarithmic scale, which explain the log-periodic oscillations of $x(t)$.

Log-periodic oscillations have been found in such diverse fields as the diffusion on random lattices,^{12,13} in dielectric relaxation¹⁴ and the magnetoresistance of ultraquantum topological materials,¹⁵ as well as in large-scale phenomena such as earthquakes¹⁶ and financial crashes.^{17,18} Following Sornette,¹⁹ they arise as a consequence of a discrete scale invariance, meaning that the scale invariance exists only for transformations $t \rightarrow \lambda t$ with discrete values of the scaling parameter λ , that is, $\lambda = \lambda_n = \kappa^n$. These relations results directly in Eq. (1), when we set $\kappa = e^{\beta E_b}$ and $\lambda_n = \tau_{1 \rightarrow n} / \tau_0$. Performing an ensemble average over many trajectories starting at $x = 0$, the theory predicts for the resulting mean position $\langle x(t) \rangle$ and mean squared displacement $\langle x^2(t) \rangle$ a power-law behavior superimposed by a weak log-oscillatory pattern.¹⁹ Showing $\langle x^2(t) \rangle$ together with the associated power law $t^{0.5}$ and its residual oscillatory part, Fig. 1d reveals that this is indeed the case for the 1D model. While power laws are the hallmark of scale-invariant and self-similar systems, the emergence of log-periodic oscillations require the discreteness of the underlying timescales.

Hence we have shown that the hierarchical structure of the 1D model approximately obeys the condition of dis-

crete scale invariance and thus gives rise to log-periodic oscillations. While this condition is indeed satisfied by various hierarchical models,^{11,12,19,20} it is less clear whether it is also obeyed by the free energy tiers of a real protein. If so, log-periodic oscillations should be observable in MD simulations as well as in time-resolved experiments. This might be indeed the case. For example, Hamm and coworkers designed photoswitchable proteins that initially trigger a local photoinduced conformational change, whose propagation through the protein can be monitored via transient infrared spectroscopy.^{21–25} Their experiments on various PDZ domains exhibited strongly nonlinear dynamics on timescales from picoseconds to tens of microseconds. Accompanying MD studies of the nonequilibrium conformational dynamics reproduced these findings and revealed a quite complex structural reorganization of the protein^{26–29} In particular, the time traces of both experiment and MD revealed overshootings, which may indicate log-periodic oscillations.³⁰

In this work we wish to explore the applicability and relevance of discrete scale invariance for the modeling and understanding of hierarchical dynamics in proteins. To this end, we first consider the above 1D system as a proof-of-principle model. As we in general rely on experimental or simulation results, we adopt a data-driven approach that does not use information on the underlying theoretical formulation of the model. Considering the time evolution of the system as input data, we aim to construct a dynamical model of the underlying dynamics. To focus first on ensemble-averaged data, we perform a timescale analysis using a maximum entropy method.^{30,31} Employing furthermore single-molecule (i.e., single-trajectory) information,³² we can recover the free-energy landscape of the model and construct a Langevin equation^{33–35} or a Markov state model.^{36–38} The analyses are shown to result in a multiexponential response function with discrete timescales, giving rise to log-periodic oscillations.

To test if the concepts are applicable to real data, we revisit the above mentioned hierarchical dynamics of the achiral peptide helix Aib₉.⁵ As the process evolves in a high-dimensional coordinate space, we first need to define collective variables that account for the hierarchically coupled degrees of freedom. Employing nonequilibrium MD simulations, we again use a timescale analysis and construct a Markov state model to identify the timescales of the process. We study the conditions under which log-periodic oscillations can be observed for Aib₉, and close with a discussion what aspects of hierarchical dynamics may be learned from these phenomena.

II. THEORY

As explained above, we wish to analyze a time series given from a nonequilibrium experiment or MD simulation, using three theoretical formulations: Maximum entropy timescale analysis,³¹ Markov state modeling,^{36–38} and discrete scale invariance.¹⁹ Moreover, we discuss if the same effects can be also observed under equilibrium

conditions.

A. Timescale analysis

The time evolution of a relaxation process can be described by a multiexponential response function

$$S(t) = s_0 - \sum_{k=1, K} s_k e^{-t/\hat{\tau}_k}, \quad (2)$$

where $S(t)$ is the considered observable of the system (e.g., $S = \langle x \rangle$ for the 1D system), which was prepared at $t=0$ in a nonequilibrium initial state (e.g., state **1** in Fig. 1b). The first term with $\hat{\tau}_0 = \infty$ gives the offset s_0 , and the time constants $\hat{\tau}_k$ ($k \geq 1$) with amplitudes s_k are given in decreasing order. To analyze the timescales inherent to a given time series $S(t)$, we determine the timescale spectrum $s(\hat{\tau}_k) \equiv s_k$. To this end, we choose the time constants to be equally distributed on a logarithmic scale (typically 10 terms per decade) and fit the corresponding amplitudes s_k to the data. When we assume that $S(t)$ is monotonic increasing, we can choose $s_k \geq 0$. The local maxima of the spectrum

$$\tau_n = \{\tau, s(\tau) = \max\} \quad (3)$$

are referred to as 'main timescales' of the process.

Equation (2) corresponds to an inverse Laplace transformation, which is an ill-posed problem, because the included exponential functions are not orthogonal to each other. To render the fitting algorithm stable, we therefore introduce an entropy-based regularization factor S_{ent} that enforces a smooth spectrum of the amplitudes s_k . This is achieved by minimizing the weighted sum $\chi^2 - \lambda_{\text{reg}} S_{\text{ent}}$ of this penalty function together with the usual root mean square deviation χ^2 of the fit function to the data.³¹ The regularization parameter λ_{reg} controls whether the model is over- or underfitted. λ_{reg} can be estimated via various criteria; see the Supplementary Material for details (Fig. S1).

B. Markov state modeling

If the free-energy landscape $\Delta G(x)$ of the system is known (e.g., from single-trajectories), we may construct a Markov state model (MSM),³⁶⁻³⁸ which describes the dynamics in terms of memory-less jumps between N metastable conformational states of the system. Assuming a timescale separation between fast intrastate fluctuations and rarely occurring interstate transitions (i.e., the Markov approximation), the dynamics of the system is completely determined by the transition matrix $T(\tau_{\text{lag}})$ containing the probabilities T_{ij} that the system jumps from state j to i within lag time τ_{lag} . Denoting the state vector at time t by $\mathbf{p}(t) = (p_1, \dots, p_N)^T$ with state probabilities p_i , the time evolution of the MSM is given by

$$\mathbf{p}(t=k\tau_{\text{lag}}) = T^k(\tau_{\text{lag}})\mathbf{p}(0). \quad (4)$$

Upon diagonalizing the transition matrix T , we obtain its left/right eigenvectors $\boldsymbol{\psi}_n^l/\boldsymbol{\psi}_n^r$ and eigenvalues μ_n . The latter yield the implied timescales

$$t_n = -\tau_{\text{lag}}/\ln \mu_n \quad (5)$$

of the system, which correspond to experimentally measurable quantities that account for the exponential decay e^{-t/t_n} associated with eigenvector $\boldsymbol{\psi}_n$. Performing an eigendecomposition of the transition matrix, the time evolution can be written as a sum of decay factors multiplied with the overlap of the eigenvectors with the initial state,³⁹

$$\mathbf{p}(t=k\tau_{\text{lag}}) = \sum_{n=0, N-1} \langle \boldsymbol{\psi}_n^r | \mathbf{p}(0) \rangle e^{-t/t_n} \boldsymbol{\psi}_n^l, \quad (6)$$

where $\boldsymbol{\psi}_0$ accounts for the equilibrium distribution associated with $t_0 = \infty$. Assuming that the observable of interest, S , adopts in state \mathbf{i} the mean value $\langle s \rangle_i$, we obtain again a multiexponential representation of the time evolution of the observable, i.e.,

$$S(t) = \sum_{i=0, N-1} \langle s \rangle_i p_i(t) = \sum_{n=0, N-1} \hat{s}_n e^{-t/t_n} \quad (7)$$

with $\hat{s}_n = \sum_i \langle s \rangle_i \langle \mathbf{i} | \boldsymbol{\psi}_n^l \rangle \langle \boldsymbol{\psi}_n^r | \mathbf{p}(0) \rangle$.³⁹ While the MSM description of $S(t)$ has the same functional form as the timescale analysis expression in Eq. (2), we note that the sum now runs over the N implied timescales t_n of the N -state system.

C. Discrete scale invariance

Following Sornette,¹⁹ we summarize the basic ideas of discrete scale invariance, which are relevant in the further discussion. A time-dependent observable $S(t)$ is said to be *scale invariant* under the transformation $t \rightarrow \lambda t$, if

$$S(t) = \mu(\lambda)S(\lambda t). \quad (8)$$

For notational convenience, the time t is given in dimensionless units. The solution of this equation follows a power law with exponent $\tilde{\alpha}$,

$$S(t) = ct^{\tilde{\alpha}}, \quad (9)$$

which can be verified by insertion. For example, the diffusion on a flat energy landscape ($U(x) = \text{const.}$) is scale invariant, that is, it looks the same on all time and length scales.

While this is in general not true for diffusion on a position-dependent potential $U(x)$, a weaker condition, *discrete scale invariance*, may apply if Eq. (8) holds at least for discrete values of the scaling parameter λ , that is,

$$\lambda = \lambda_n = \kappa^n \quad (n \in \mathbb{N}), \quad (10)$$

where κ is the fundamental scaling ratio. This condition reflects a symmetry of the problem, such as a lattice

potential or the above considered hierarchical landscape. Inserting Eq. (10) in (8), we obtain

$$\mu\lambda^{\tilde{\alpha}} = 1 = e^{i2\pi m} \quad (m \in \mathbb{Z}), \quad (11)$$

where the second equation indicates that the exponent is in general complex valued and can be written as

$$\tilde{\alpha} = -\frac{\ln \mu}{\ln \lambda} + i\frac{2\pi m}{\ln \lambda} \equiv \alpha + i\omega. \quad (12)$$

Using $t^{i\omega} = e^{i\omega \ln t}$ and assuming that $S = \text{Re } S$, we obtain

$$S(t) = ct^\alpha \cos(\omega \ln t), \quad (13)$$

indicating that $S(t)$ exhibits log-periodic oscillations. Assuming discrete scale invariance [Eq. (10)], the frequency ω depends only on the fundamental scaling ratio κ ,

$$\omega = \frac{m2\pi}{n \ln \kappa} = \frac{2\pi}{\ln \kappa}, \quad (14)$$

because m is an arbitrary integer, which can be chosen as $m = n$. This is in contrast to the case of general scale invariance (where λ can take an arbitrary value), which results in a frequency $\omega \propto 1/\ln \lambda$ that is not constant. Hence, the existence of the log-oscillations rests on the existence of discrete scaling parameters $\lambda_n = \kappa^n$.

Let us apply the above theory to our hierarchical model introduced in Fig. 1b. Showing consecutive barriers of similar height βE_b , the system is expected to approximately exhibit transition times, $\tau_{1 \rightarrow n} = \tau_0 e^{(n-1)\beta E_b}$, that are discrete and equidistant on a logarithmic scale, see Eq. (1). Associating these timescales with the scaling parameter via

$$\lambda_n = e^{n\beta E_b}, \quad (15)$$

we obtain for the fundamental scaling ratio

$$\kappa = e^{\beta E_b}, \quad (16)$$

which is inverse proportional to the probability to cross single barrier. Introducing $\tau_{\log} = \log e \, 2\pi/\omega$, we find from Eqs. (14) and (16)

$$\tau_{\log} = \beta E_b \log e \quad (17)$$

(with $\log e \approx 0.43$), stating that the period of the oscillations in decadic log time directly reflects the average barrier height of the hierarchical energy landscape.

When we consider a time trace $S(t)$ obtained from an experiment or MD simulation, we generally do not know the underlying energy landscape and the corresponding transition times. Nonetheless, we may perform a timescale analysis [Eq. (3)] to obtain the main exponential timescales $\tau_1 \geq \tau_2 \geq \tau_3 \dots$. In direct analogy to Eq. (1), the existence of log-oscillations then requires that these timescales are equally spaced by their period τ_{\log} ,

$$\log \tau_n - \log \tau_{n+1} = \tau_{\log}. \quad (18)$$

Note that this condition is certainly fulfilled in the common case that only two main timescales exist, τ_1 and τ_2 . When we associate τ_2 with the crossing of the first barrier βE_1 and τ_1 with the timescale of the barrier βE_{tot} of the overall transition, we obtain from our simple rate-theory consideration

$$\tau_{\log} = \beta(E_{\text{tot}} - E_1) \log e \quad (19)$$

stating that the log-period reflects the energy difference of the overall and initial barriers.

Since the barrier heights of a 1D energy landscape do not necessarily reflect the true reaction rates of a multi-dimensional system,⁴⁰ in general we cannot directly associate τ_{\log} with specific barriers of the system. Rather the energy $\Delta E = \tau_{\log}/(\beta \log e)$ reflects an overall roughness of the energy landscape, which gives rise to an effective diffusion coefficient or intramolecular friction of the process.^{9,41-43}

D. Modeling log-periodic power laws

To be able to fit given MD data to a log-periodic power law $S(t)$, we generalize Eq. (13) to the functional form

$$S(t) = s_a + s_b t^\alpha + s_c t^\alpha \cos\left(\frac{2\pi}{\tau_{\log}} \log t + \varphi\right), \quad (20)$$

which introduces the amplitudes s_b and s_c and the phase φ defining the oscillations, and the initial value s_a , which is chosen such that $S(t) > 0$. To discuss the oscillations, we also consider the oscillatory residual, defined as

$$R(t) = (S(t) - s_a)t^{-\alpha}. \quad (21)$$

It is instructive to study to what extent a simple multiexponential model $S(t) = \sum_n s_n e^{-t/\tau_n}$ with only two or three main timescales τ_n and associated amplitudes s_n can give rise to the log-periodic power law in Eq. (20). To this end, Fig. S2 shows power-law fits for models with various choices of the timescales and amplitudes. Using two timescales that are more than one decade apart, i.e., $\log \tau_1 - \log \tau_2 \equiv \Delta_{12} \gtrsim 1$, we obtain two well-defined log-oscillations with $\tau_{\log} \approx \Delta_{12}$ for various choices of the amplitudes. On the other hand, if the timescales are too close to each other ($\Delta_{12} < 1$), we effectively see only a single exponential term without log-oscillations. The scenario is similar for three timescales. If the timescale are roughly logarithmically equidistant and well separated, i.e., $\Delta_{12} \approx \Delta_{23} \gtrsim 1$, we obtain three well-defined log-oscillations. If two of the timescales are too close to each other, we find only two exponential terms and two log-oscillations.

E. Nonequilibrium vs. equilibrium conditions

In the discussion above, we have assumed nonequilibrium initial conditions, i.e., we initially prepared the system in a nonstationary state. This raises the question, if

the same effects can be observed under equilibrium conditions. Assuming linear response conditions, for example, the nonequilibrium time evolution of the ensemble average $\langle x(t) \rangle$ is known to be closely related to the auto-correlation function

$$C(t) = \langle \delta x(t) \delta x(0) \rangle_{\text{eq}} / \langle \delta x^2 \rangle_{\text{eq}}, \quad (22)$$

where $\delta x = x - \langle x \rangle$ and $\langle \dots \rangle$ denotes a time average over an equilibrium trajectory.⁴⁴ In the nonequilibrium set-up considered in Fig. 1, however, we typically stop the experiment or simulation, once the system reaches the final state **4**. In this way, we prevent the reverse reaction out of this state and the subsequent propagation of the system, which would occur under equilibrium conditions. The reverse reaction may introduce additional timescales that are not encountered in the forward reaction. Moreover, the nonequilibrium preparation results in well-defined initial conditions for the climb over the energy landscape, which may lead to an oscillatory behavior of the nonequilibrium ensemble average $\langle x(t) \rangle$. On the other hand, the averaging over an equilibrium trajectory may average over these oscillations.

III. DISCUSSION OF THE 1D MODEL

A. Methods

Employing the 1D energy landscape $U(x)$ shown in Fig. 1b, simulations of the Langevin equation $m\ddot{x}(t) = -\frac{dU(x)}{dx} - \Gamma\dot{x}(t) + K\xi(t)$ were performed as described in Ref. 11. Specifically, we used a mass of $m = 1$ u, constant friction ($\Gamma = 130$ kJ ps/mol) and noise amplitude ($K = 25$ kJ ps^{1/2}/mol), δ -correlated Gaussian noise ξ of zero mean, and a temperature $T = 300$ K. Collecting the data $x(t)$ every $\delta t = 0.4$ ps, we transformed to logarithmically spaced data for easier representation. To remove fast fluctuations, a Gaussian filter with a standard deviation of 6 frames is used. Starting at $x = 0$, in total $N = 3000$ trajectories were run until they reach state **4**, i.e., for $x \geq 12.3$. To calculate the mean position $\langle x(t) \rangle$, we performed an ensemble average over the N trajectories, where the initial conditions of the individual trajectories were sampled from a Boltzmann velocity distribution. When we calculate the energy profile $\Delta G(x) = -k_B T P(x)$ from the resulting probability distribution $P(x)$, we consistently recover the potential energy $U(x)$.⁴⁵ Showing the convergence of the mean position $\langle x(t) \rangle$ with the sample size N , Figs. S3a,b reveal a smooth increase of $\langle x(t) \rangle$ for $N \gtrsim 10^3$, while for $N \lesssim 10^2$ we find additional high-frequency fluctuations as signatures of transitions of individual trajectories. This indicates that an incomplete sampling of the stochastic process can be easily misinterpreted as log-periodic oscillations of $\langle x(t) \rangle$.

As the 1D model in Fig. 1b is well characterized in terms of its states **1** to **4**, we may construct a MSM,^{36–38} using our open-source Python package `msmhelper`.⁴⁶ To

this end, we first apply a Gaussian smoothing with a standard deviation of 2.4 ps to the individual trajectories $x(t)$.⁴⁷ To avoid problems at the boundaries, we define the states via their cores^{48–50} (gray regions in Fig. 1b), that is, we assign states **1** to **4** to the x -regions $[-0.6, 0.7]$, $[3.6, 5.8]$, $[9.2, 10.8]$, and $x \geq 12.3$. Intermediate frames between these regions are assigned to the last populated state. The resulting state trajectories are then directly employed to calculate the transition matrix $T(\tau_{\text{lag}})$. Due to the coring procedure and since the underlying dynamics was generated by a Markovian Langevin equation, we expect the Markov approximation to hold well. As a consequence, the implied timescales of the 4-state model are constant already at lag time $\tau_{\text{lag}} = \delta t$, and the resulting Chapman-Kolmogorov equation (4) holds accurately, see Figs. S3c,d.

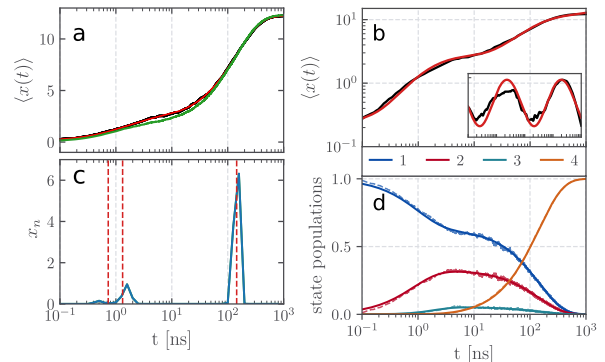


FIG. 2. Analysis of the 1D model shown in Fig. 1b. (a) Mean position $\langle x(t) \rangle$, as obtained from (black) the Langevin simulations, (red) the fit of the timescale analysis [(Eq. (2)), and (green) the MSM [(Eq. (7))]. (b) Double-logarithmic representation of $\langle x(t) \rangle$ (black) together with the fit to Eq. (18) (red), showing the oscillatory residual $R(t)$ [Eq. (21)] in the enclosure. (c) Timescale spectrum [Eq. (2), in blue], compared to the implied timescales [Eq. (5), in red] of an MSM constructed from the Langevin data. (d) Time evolution of the state probabilities $p_n(t)$ of the MSM (thick lines) and the Langevin data (thin dashed lines).

B. Results

As detailed above, we run $N = 3000$ Langevin simulations that start at time $t = 0$ in state **1**, and follow them until they reach the final state **4**. Figures 2a,b show the time evolution of the resulting mean position $\langle x(t) \rangle$ in log-time and double-log representation, which reflects the gradual climb over the staircase-shaped energy landscape. To identify the timescales of this climb, we model the time evolution of $\langle x(t) \rangle$ by the multiexponential response function in Eq. (2), see Methods. The resulting maximum-entropy timescale spectrum ($\lambda_{\text{reg}} = 10$) shown in Fig. 2c exhibits two main timescales at $\tau_1 = 160$ ns and $\tau_2 = 1.6$ ns, and a rather weak signature at 0.5 ns. From the time evolution of the individual trajectories

(Fig. 1c), we conclude that the short timescale reflects first attempts to cross the barrier to state **2**, while the long timescale accounts for transitions to the final state **4**.

From a data-driven view, the above timescale analysis requires only ensemble-averaged data [e.g., $\langle x(t) \rangle \propto \sum_n x_n(t)$]. If single-trajectory information [i.e., $x_n(t)$] is available,³² we can calculate the probability distribution along x and thus recover the energy landscape $\Delta\mathcal{G}(x) = -k_B T \ln P(x)$ of the model. By identifying the four metastable conformational states **1** to **4** of the system, we may then construct a MSM of the dynamics (see Methods). As expected for a simple 1D system, we find that the resulting implied timescales of the MSM, $t_1 = 145$ ns, $t_2 = 1.3$ ns and $t_3 = 0.7$ ns, agree well with the main peaks of the timescale spectrum in Fig. 2c.

What is more, the MSM provides an explanation of these timescale in terms of the population flux between the states. Showing the time evolution of the population probabilities $p_i(t)$ of the four states, Fig. 2d reveals that the population of initial state **1** decays (within all three timescales t_3 , t_2 and t_1) such that the intermediate states **2** and **3** are transiently populated (within t_3 and t_2), until the system relaxes in final state **4** (within t_1). When we compare the time evolution of the state populations obtained from the MSM to the Langevin results, we find excellent agreement. Moreover, the MSM calculation of the mean position $\langle x(t) \rangle$ via Eq. (7) matches perfectly the reference results (Fig. 2a).

Interestingly, we find that the fastest timescale $t_3 = 0.7$ ns clearly shows up in the initial decay of $p_1(t)$ and the corresponding initial rise of $p_2(t)$, although it is hardly visible in the timescale analysis in Fig. 2c. This reflects the fact that the MSM exploits the structure of the energy landscape, while the timescale analysis only uses the evolution of the observable $\langle x(t) \rangle$, and thus depends considerably on the definition of the collective coordinate x .

We are now in a position to assess if the dynamics of the 1D problem fulfills the conditions of discrete scale invariance and therefore gives rise to a log-periodic power law. Figure 2c shows that both timescale analysis and MSM essentially yield only two timescales, 160 ns and 1.6 ns. (The third MSM timescale carries hardly any amplitude and can be omitted.) Alternatively, we may calculate the average transition times $\tau_{1 \rightarrow n}$ to reach state n after starting in state **1**, yielding $\tau_{1 \rightarrow 2} = 2.6$ ns, $\tau_{1 \rightarrow 3} = 23$ ns and $\tau_{1 \rightarrow 4} = 147$ ns. As $\tau_{1 \rightarrow 3}$ can be neglected (because state **3** is hardly populated, see Fig. 2d), we are again left with two times, which resemble closely the timescales determined by timescale analysis and the MSM. Because Eq. (18) is directly fulfilled if only two timescales exist, the 1D problem is expected to show typical phenomena associated with discrete scale invariance.

Using $\tau_1 = 160$ ns and $\tau_2 = 1.6$ ns, Eq. (18) predicts a log-periodic power law with an a period of $\tau_{\log} = 2.0$. To test these predictions, we use the functional form in Eq.

(20) and fit the Langevin data to a log-periodic power law. Figure 2b shows that we obtain a perfect fit, when we use $\tau_{\log} = 1.92$ for the period, $\alpha = 0.31$ for the exponent, and the coefficients $s_a = -0.5$, $s_b = 1.7$, $s_c = -0.2$, and $\varphi = 1.9$. The good agreement of theoretical [Eq. (18)] and fitted values for τ_{\log} is also reflected in the fact that the maxima of the log-periodic oscillation coincide well with the peaks of the timescale spectrum in Fig. 2c.

Moreover, Eq. (19) allows us to infer from the period $\tau_{\log} = 2$ an effective roughness $\beta\Delta E = 4.7$ of the underlying energy landscape. In the case of only two timescales, $\beta\Delta E$ can be interpreted as the energy difference of the the overall and initial barriers. Indeed the energy difference $\beta\Delta E = 4.5$ obtained from the potential $U(x)$ in Fig. 1b agrees well with the theoretical prediction. When we employ the simple rate approximation of Eq. (15), we may also relate τ_{\log} to the average barrier height βE_b of the hierarchical energy landscape via Eq. (17). In fact, $\beta E_b = 3.8$ obtained from the potential $U(x)$ in Fig. 1b matches $\beta\Delta E = 4.7$ at least qualitatively.

Apart from considering the mean $\langle x(t) \rangle$, it is interesting to discuss the mean squared displacement $\langle x^2(t) \rangle$, which accounts for the diffusional motion of the system. As shown in Fig. 1d, we obtain similar log-oscillations with $\tau_{\log} = 1.72$ and an increase of the power-law exponent to $\alpha = 0.5$. That is, the hierarchical dynamic of the 1D model manifest itself in subdiffusion, which reflects the roughness of the underlying energy landscape.^{1,9}

So far, we have assumed a nonequilibrium preparation of the system in the initial state **1**. To test if the same effects can be observed under equilibrium conditions, we run a 16 μ s-long equilibrium simulation of the 1D model and calculate the autocorrelation function $C(t)$ in Eq. (22). Figure S4 shows that $C(t)$ decays on the timescales $\tau_1 = 26$ ns and $\tau_2 = 1.3$ ns. While τ_2 is similar to the implied timescale t_2 found in the nonequilibrium case, τ_1 is significantly shorter than the nonequilibrium timescale $t_1 = 160$ ns, which reflects the possibility of back-reaction from state **4**. Moreover, we find that the equilibrium autocorrelation function shows no evidence of log-periodic oscillations. This indicates that the discrete scale invariance of the observable $\langle x(t) \rangle$ requires well-defined initial conditions (as given by a nonequilibrium preparation) as well as a well-defined end state, which prevent the averaging over the oscillations.

IV. HIERARCHICAL DYNAMICS OF A PEPTIDE HELIX

It is interesting to study to what extent the theoretical concepts established above for the 1D model can be transferred to the analysis of all-atom MD data. As a well-established model system,^{5,51–53} we consider the achiral peptide Aib₉ that undergoes complete left- to right-handed chiral transitions of the helix, see Fig. 3a.

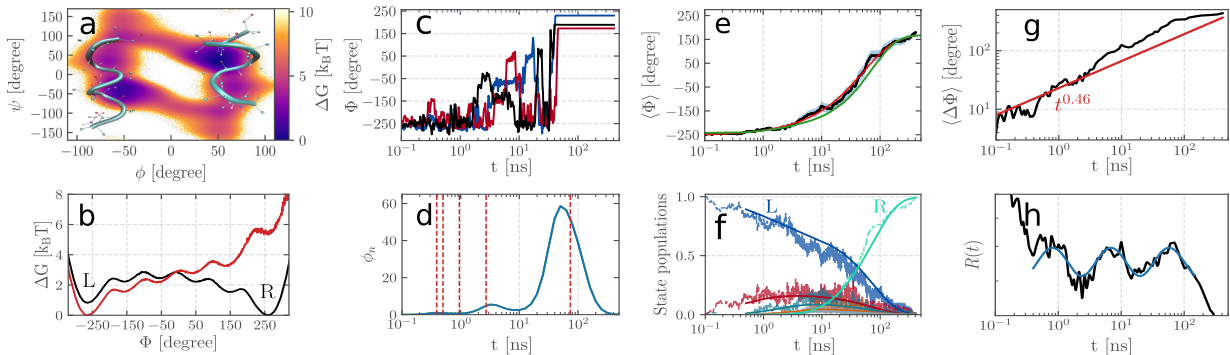


FIG. 3. Hierarchical dynamics of the peptide helix Aib₉. (a) Structure of the left-handed and right-handed conformation of Aib₉, along with the Ramachandran plot $\Delta G(\phi, \psi)$, averaged over the five inner peptide residues. (b) Energy landscapes along the collective coordinate Φ [Eq. (23)], obtained from equilibrium MD simulations⁵ (black) and from nonequilibrium trajectories that exhibit a single L \rightarrow R transition (red).⁵⁴ (c) Time evolution of three individual nonequilibrium trajectories $\Phi(t)$. (d) Timescale spectrum [Eq. (2), in blue], compared to the implied timescales [Eq. (5), in red] of an MSM constructed from the MD data. (e) Mean position $\langle \Phi(t) \rangle$, as obtained from (black) the nonequilibrium MD trajectories, (red) the fit of the timescale analysis [(Eq. (2))], and (green) the MSM [(Eq. (7))]. (f) Time evolution of the state probabilities $p_n(t)$ of the MSM. (g) Double-logarithmic representation of $\langle \Delta \Phi(t) \rangle = \langle \Phi(t) \rangle + 255^\circ$ together with the associated power law $t^{0.46}$ and (h) the residual oscillatory part $R(t)$ [Eq. (21)].

A. Model and methods

Buchenberg et al.⁵ performed extensive MD simulations of Aib₉ (H₃C-CO-(NH-C_α(CH₃)₂-CO)₉-CH₃), using the GROMACS program suite⁵⁵ with the GROMOS96 43a1 force field⁵⁶ and explicit chloroform solvent.⁵⁷ Here we use eight of their MD trajectories at 320 K of each 2 μ s length, using a time step $\Delta t = 1$ ps. The resulting Ramachandran plot $\Delta G(\phi_i, \psi_i)$ along the backbone dihedral angles (ϕ_i, ψ_i) of the five inner peptide residues ($i = 3, \dots, 7$) reveals a point symmetry with respect to (0,0), which shows that Aib₉ indeed samples both left-handed ($\phi_i \geq 0$) and right-handed ($\phi_i \leq 0$) conformations with similar probability (Fig. 3a). The corresponding two local conformational states l at $\approx (-50^\circ, -45^\circ)$ and r at $(50^\circ, 45^\circ)$ correspond to a right- and left-handed helix, respectively.⁵⁴ The ring-shaped free energy landscape ΔG reveals that left- to right-handed transitions l \leftrightarrow r of a single residue along dihedral angle ϕ_i first requires a transition along dihedral angle ψ , which occurs about 10 times faster than l \leftrightarrow r transitions occurring on a 1 ns timescale. On the other hand, left- to right-handed chiral transitions of the entire helix, L \leftrightarrow R, requires individual l \leftrightarrow r transition of all residues, which occur on a 100 ns timescale.

In the following, we focus on this last tier of the hierarchical dynamics and study the L \rightarrow R transition, represented by the sum of the ϕ_i angles of the five inner residues,

$$\Phi = \sum_{i=3,7} \phi_i. \quad (23)$$

It was shown in Ref. 5 that Φ is equivalent to the first component of a principal component analysis of all backbone dihedral angles.⁵⁸ Figure 3b shows the resulting free

energy landscape $\Delta G(\Phi)$ obtained from the equilibrium MD simulations.⁵⁴ Adopting a product-state notation of the five inner residues, we note that the two main minima L = (lllll) and R = (rrrrr), are connected by four intermediate states with an increasing number of r-residues, e.g., (rllll), (rllll), (rrlll) and (rrrrl). As discussed elsewhere,⁵² the free energy difference ($\sim 1k_B T$) between the states L and R is not due to incomplete sampling but is caused by an inaccuracy of the force field parameterization of Aib₉, which is not of interest here.

As discussed in Sec. II E, the observation of log-periodic oscillations along Φ requires a nonequilibrium preparation and monitoring of the system (rather than equilibrium simulations that average over these oscillations). To this end, we extracted all L \rightarrow R transitions occurring during the $8 \times 2 \mu$ s MD simulations (see the Supplementary Material for details). Starting when the system enters state L, monitoring the transition to state R, and ending when it reaches R, we thus obtain 63 independent nonequilibrium trajectories, which are used in the subsequent analysis. Calculating the probability distribution $P(\Phi)$ from these trajectories, the resulting energy landscape $\Delta \mathcal{G}(\Phi) = -k_B T P(\Phi)$ is shown in Fig. 3b. Since each state along $\Delta \mathcal{G}(\Phi)$ serves as prerequisite for the overall L \rightarrow R transition, the energy landscape shows again the typical staircase shape, quite similar as anticipated by the 1D model. For Aib₉, the first and last barriers have a height of ~ 1.7 and $2.4 k_B T$, the three intermediate barriers of $\sim 0.8 k_B T$. In contrast to the 1D model, however, the energy landscape $\Delta \mathcal{G}(\Phi)$ of Aib₉ represents a projection of a high-dimensional system on a 1D coordinate. As a consequence, for example, the states along Φ may consist of various substates [e.g., the first intermediate state contains the conformations (rllll), (lr-

lll), (llrll), (lllrll), (llllr)], which renders the microscopic interpretation of the barriers along Φ difficult.⁴⁰

B. Results

Considering the time evolution of three individual trajectories $\Phi(t)$, Fig. 3c shows the gradual climbing of the energy landscape $\Delta\mathcal{G}(\Phi)$, starting from the initial state L until the final state R is reached. By averaging over all trajectories, we obtain the mean position $\langle\Phi(t)\rangle$, which is seen to raise within 100 ns (Fig. 3e). This is in line with the timescale analysis in Fig. 3d (using the regularization parameter $\lambda_{\text{reg}} = 0.5$), which reveals peaks at $\tau_1 = 51$ ns, $\tau_2 = 3.2$ ns, and a weak feature at $\tau_3 = 0.4$ ns. The resulting multiexponential fit of $\langle\Phi(t)\rangle$ via Eq. (2) is found to be in excellent agreement with the MD data (Fig. 3e).

Next we construct a MSM of the system, by considering the six minima of $\Delta\mathcal{G}(\Phi)$ as metastable conformational states, see the Supplementary Material for details. Choosing a lag time of 0.5 ns, the resulting implied timescales t_n of the MSM are 74, 2.7, 1.0, 0.5, and 0.4 ns (Fig. S5a), which agree qualitatively with the peaks of the timescale analysis (Fig. 3d). Calculating the population probabilities $p_i(t)$ of the five states, the results of MD and MSM are in excellent agreement (Fig. 3f), at least within the relatively large fluctuations of the MD data caused by finite sampling. Moreover, the MSM calculation of the mean position $\langle\Phi(t)\rangle$ via Eq. (7) matches perfectly the MD results (Fig. 3e). From the time evolution of the state populations in Fig. 3f, we see a multiscale decay of the initial state L such that intermediate states are transiently populated (within t_4 , t_3 , and t_2), until the system relaxes in final state (within t_1). The average transition times from state L to the various intermediate states and the final state R are calculated as 0.8, 6.9, 25, 48, and 73 ns, respectively.

We finally turn to the discussion of the discrete scale invariance of the hierarchical dynamics of Aib₉. Since the MSM involves additional assumptions (such as the choice of the conformational metastable states), we base the discussion on the timescales determined by the maximum-entropy timescale analysis: $\tau_1 = 51$ ns, $\tau_2 = 3.2$ ns, and $\tau_3 = 0.4$ ns. By calculating the differences $\log \tau_1 - \log \tau_2 = 1.2$ and $\log \tau_2 - \log \tau_3 = 0.91$, we find that the logarithmic timescales are approximately equally spaced. From this, Eq. (18) predicts a log-periodic power law with an a period of $\tau_{\text{log}} \approx 1$. On the other hand, when we fit the MD data to a log-periodic power law [Eq. (20)], we obtain $\tau_{\text{log}} = 0.93$ for the period (as well as $\alpha = 0.46$ for the exponent, and the coefficients $s_a = -23$, $s_b = 45$, $s_c = -4.1$, and $\varphi = -2.5$). This good agreement of theory and fit for τ_{log} is reflected in the matching of the peaks of the log-oscillation and the main timescales of the dynamics.

When we use Eq. (19) to calculate from the period $\tau_{\text{log}} = 1$ the effective roughness of the underlying energy landscape, we obtain $\beta\Delta E = 2.3$. Compared to the energy landscape $\Delta\mathcal{G}(\Phi)$ in Fig. 3b, this value is smaller

than the energy difference of the overall and initial barriers, $\beta\Delta E = 4$, and larger than the average barrier height, $\beta E_b = 1.3$. This again demonstrates that barrier heights obtained from a 1D projection of the energy landscape in general cannot be directly associated with the true reaction rates of a multidimensional system.

V. DISCUSSION AND CONCLUSION

The emergence of discrete scale invariance and the associated phenomenon of log-periodic oscillations in protein relaxation dynamics rests on the existence of logarithmically spaced discrete timescales of the process. Adopting a 1D model as well as MD data of a peptide conformational transition, here we have outlined a scenario that explains these findings in terms of a simple hierarchical mechanism.

Consider a global structural rearrangement of a protein, which involves the change of several inter-dependent local interactions. A simple example is the unzipping of a β -sheet which involves the braking of adjacent hydrogen (H) bonds. Initially, the first H-bond is less stabilized by the β -sheet and therefore opens and closes frequently. Once it is open, it is easier for the next H-bond to open, which in turn facilitates the opening of the following H-bond. This continues until the β -sheet is completely unzipped and the resulting state is stabilized (e.g., by entropic effects or by forming other bonds). Less likely but also possible is that some of the inner H-bonds opens first and start the unzipping process this way. At any rate, we find that the inter-dependence of the consecutive H-bonds gives rise to a hierarchical mechanism, where several fast local conformational transitions are a prerequisite for a slow global transition to occur. Essentially the same picture is obtained, when we consider the global left- to right-handed transition of the peptide helix Aib₉, which requires local chiral transitions of each individual amino acid.

To describe the global transition by a 1D reaction coordinate, we define the sum of the distances of the individual H-bonds as a collective coordinate. Assuming that the activation energy to break a single H-bond is given by βE_B , the scenario gives a staircase-like free energy landscape shown in Fig. 1b, where the consecutive energy barriers are of similar height. While in a non-interacting scheme the energy barrier of all steps would be the same, the barrier heights of the hierarchically coupled subprocesses may vary due to the mutual interactions. (E.g., the first and last barrier is larger in Fig. 3b.) We note that the characteristic staircase shape of the energy landscape and the stabilized end states are a consequence of the hierarchical interactions of the problem.

Considering the time evolution of the hierarchical model, we expect a gradual climb of the consecutive energy barriers until the final state is reached. Although the staircase-like energy landscape appears to suggest a sequential mechanism, the process may as well occur co-

operatively. In fact, we find for both systems that successful global transitions typically climb the energy landscape without stopping in an intermediate state. Employing maximum entropy-based timescale analysis and Markov state modeling, we have shown that the hierarchical mechanism gives rise to two or three discrete timescales that are roughly equidistant in log-time. According to discrete scale invariance theory, the resulting response functions exhibit a power-law behavior that is superimposed by log-oscillations with a period τ_{\log} . Remarkably, these oscillations are a direct consequence of the hierarchical model. In particular, we have shown that the period τ_{\log} of the log-oscillations directly reflects the effective roughness of the underlying energy landscape, which in simple cases can be interpreted in terms of its barrier heights. That is, by measuring the logarithmic period in an ensemble-averaged experiment or MD simulation, we may conclude on the structure of the hierarchical free energy landscape.

In ongoing work, we wish to apply the approach to the investigation of allosteric transitions in proteins.⁵⁹ For example, a joint experimental and MD study of the structural response of a PDZ2 domain revealed four logarithmically equidistant timescales and complex spectroscopic and simulated time traces.²² While the system may provide a challenge for a discrete scale invariance analysis, it could shed light on the elusive nature of allosteric communication.

Supplementary material

Supplementary methods including details of the timescale analysis and the MSM, and supplementary results including additional data for the 1D model and of Aib₉.

Acknowledgments

The authors thank Peter Hamm, Dima Makarov, Daniel Nagel, Steffen Wolf and Benjamin Lickert for helpful comments and discussions. This work has been supported by the Deutsche Forschungsgemeinschaft (DFG) within the framework of the Research Unit FOR 5099 "Reducing complexity of nonequilibrium" (project No. 431945604), the High Performance and Cloud Computing Group at the Zentrum für Datenverarbeitung of the University of Tübingen, the state of Baden-Württemberg through bwHPC and the DFG through grant no INST 37/935-1 FUGG (RV bw16I016), and the Black Forest Grid Initiative.

Data availability

All data shown are available on reasonable request.

¹X. Hu, L. Hong, M. Dean Smith, T. Neusius, X. Cheng, and J. C. Smith, The dynamics of single protein molecules is nonequilibrium and self-similar over thirteen decades in time, *Nat. Phys.* **12**, 171 (2016).

- ²K. Lindorff-Larsen, P. Maragakis, S. Piana, and D. E. Shaw, Picosecond to millisecond structural dynamics in human ubiquitin, *J. Phys. Chem. B* **120**, 8313 (2016).
- ³Q. Cui and I. Bahar, *Normal Mode Analysis*, Chapman & Hall, London, 2006.
- ⁴R. G. Palmer, D. L. Stein, E. Abrahams, and P. W. Anderson, Models of hierarchically constrained dynamics for glassy relaxation, *Phys. Rev. Lett.* **53**, 958 (1984).
- ⁵S. Buchenberg, N. Schaudinnus, and G. Stock, Hierarchical biomolecular dynamics: Picosecond hydrogen bonding regulates microsecond conformational transitions, *J. Chem. Theory Comput.* **11**, 1330 (2015).
- ⁶H. Frauenfelder, S. Sligar, and P. Wolynes, The energy landscapes and motions of proteins, *Science* **254**, 1598 (1991).
- ⁷K. A. Dill and H. S. Chan, From Levinthal to pathways to funnels: The "new view" of protein folding kinetics, *Nat. Struct. Bio.* **4**, 10 (1997).
- ⁸K. A. Henzler-Wildman, M. Lei, V. Thai, S. J. Kerns, M. Karplus, and D. Kern, A hierarchy of timescales in protein dynamics is linked to enzyme catalysis, *Nature (London)* **450**, 913 (2007).
- ⁹L. Milanese, J. P. Waltho, C. A. Hunter, D. J. Shaw, G. S. Beddard, G. D. Reid, S. Dev, and M. Volk, Measurement of energy landscape roughness of folded and unfolded proteins, *Proc. Natl. Acad. Sci. USA* **109**, 19563 (2012).
- ¹⁰G. G. Maisuradze, A. Liwo, P. Senet, and H. A. Scheraga, Local vs global motions in protein folding, *J. Chem. Theory Comput.* **9**, 2907 (2013).
- ¹¹B. Lickert, S. Wolf, and G. Stock, Data-driven Langevin modeling of nonequilibrium processes, *J. Phys. Chem. B* **125**, 8125 (2021).
- ¹²J. Bernasconi and W. R. Schneider, Diffusion in a one-dimensional lattice with random asymmetric transition rates, *J. Phys. A: Math. and Gen.* **15**, L729 (1982).
- ¹³J. Klafter, G. Zumofen, and A. Blumen, On the propagator of Sierpinski gaskets, *J. Phys. A: Math. and Gen.* **24**, 4835 (1991).
- ¹⁴A. Khamzin, R. Nigmatullin, and I. Popov, Log-periodic corrections to the Cole-Cole expression in dielectric relaxation, *Physica A* **392**, 136 (2013).
- ¹⁵H. Wang et al., Discovery of log-periodic oscillations in ultra-quantum topological materials, *Sci. Adv.* **4**, eaau5096 (2018).
- ¹⁶Didier Sornette and Charles G. Sammis, Complex critical exponents from renormalization group theory of earthquakes: Implications for earthquake predictions, *J. Phys. I France* **5**, 607 (1995).
- ¹⁷A. Johansen, O. Ledoit, and D. Sornette, Crashes as critical points, *Int. J. Theor. Applied Finance* **03**, 219 (2000).
- ¹⁸P. Geraskin and D. Fantazzini, Everything you always wanted to know about log periodic power laws for bubble modelling but were afraid to ask, *Eur. J. Finance* **19**, 366 (2013).
- ¹⁹D. Sornette, Discrete-scale invariance and complex dimensions, *Phys. Rep.* **297**, 239 (1998).
- ²⁰R. Metzler, J. Klafter, and J. Jortner, Hierarchies and logarithmic oscillations in the temporal relaxation patterns of proteins and other complex systems, *Proc. Natl. Acad. Sci. USA* **96**, 11085 (1999).
- ²¹B. Buchli, S. A. Waldauer, R. Walser, M. L. Donten, R. Pfister, N. Bloechliger, S. Steiner, A. Caffisch, O. Zerbe, and P. Hamm, Kinetic response of a photoperperturbed allosteric protein, *Proc. Natl. Acad. Sci. USA* **110**, 11725 (2013).
- ²²O. Bozovic, C. Zanobini, A. Gulzar, B. Jankovic, D. Buhrke, M. Post, S. Wolf, G. Stock, and P. Hamm, Real-time observation of ligand-induced allosteric transitions in a PDZ domain, *Proc. Natl. Acad. Sci. USA* **117**, 26031 (2020).
- ²³O. Bozovic, B. Jankovic, and P. Hamm, Sensing the allosteric force, *Nat. Commun.* **11**, 5841 (2020).
- ²⁴O. Bozovic, J. Ruf, C. Zanobini, B. Jankovic, D. Buhrke, P. J. M. Johnson, and P. Hamm, The Speed of Allosteric Signaling Within a Single-Domain Protein., *J. Phys. Chem. Lett.* **12**, 4262 (2021).

- ²⁵O. Bozovic, B. Jankovic, and P. Hamm, Using azobenzene photocontrol to set proteins in motion, *Nat. Rev. Chem.* **6**, 112 (2022).
- ²⁶P. H. Nguyen, R. D. Gorbunov, and G. Stock, Photoinduced conformational dynamics of a photoswitchable peptide: A nonequilibrium molecular dynamics simulation study, *Biophys. J.* **91**, 1224 (2006).
- ²⁷S. Buchenberg, V. Knecht, R. Walser, P. Hamm, and G. Stock, Long-range conformational transition in a photoswitchable allosteric protein: A molecular dynamics simulation study, *J. Phys. Chem. B* **118**, 13468 (2014).
- ²⁸S. Buchenberg, F. Sittel, and G. Stock, Time-resolved observation of protein allosteric communication, *Proc. Natl. Acad. Sci. USA* **114**, E6804 (2017).
- ²⁹A. A. I. Ali, A. Gulzar, S. Wolf, and G. Stock, Nonequilibrium modeling of the elementary step in PDZ3 allosteric communication, *J. Phys. Chem. Lett.* **13**, 9862 – 9868 (2022).
- ³⁰G. Stock and P. Hamm, A nonequilibrium approach to allosteric communication, *Phil. Trans. B* **373**, 20170187 (2018).
- ³¹V. A. Lórenz-Fonfría and H. Kandori, Transformation of time-resolved spectra to lifetime-resolved spectra by maximum entropy inversion of the Laplace transform, *Appl. Spectrosc.* **60**, 407 (2006).
- ³²A. M. Berezhkovskii and D. E. Makarov, From nonequilibrium single-molecule trajectories to underlying dynamics, *J. Phys. Chem. Lett.* **11**, 1682 (2020).
- ³³O. F. Lange and H. Grubmüller, Collective Langevin dynamics of conformational motions in proteins, *J. Chem. Phys.* **124**, 214903 (2006).
- ³⁴R. Hegger and G. Stock, Multidimensional Langevin modeling of biomolecular dynamics, *J. Chem. Phys.* **130**, 034106 (2009).
- ³⁵C. Ayaz, L. Tepper, F. N. Brüning, J. Kappler, J. O. Daldrop, and R. R. Netz, Non-Markovian modeling of protein folding, *Proc. Natl. Acad. Sci. USA* **118**, e2023856118 (2021).
- ³⁶G. R. Bowman, V. S. Pande, and F. Noé, *An Introduction to Markov State Models*, Springer, Heidelberg, 2013.
- ³⁷W. Wang, S. Cao, L. Zhu, and X. Huang, Constructing Markov state models to elucidate the functional conformational changes of complex biomolecules, *WIREs Comp. Mol. Sci.* **8**, e1343 (2018).
- ³⁸F. Noé and E. Rosta, Markov models of molecular kinetics, *J. Chem. Phys.* **151**, 190401 (2019).
- ³⁹F. Noé, S. Doose, I. Daidone, M. Löllmann, M. Sauer, J. D. Chodera, and J. C. Smith, Dynamical fingerprints for probing individual relaxation processes in biomolecular dynamics with simulations and kinetic experiments, *Proc. Natl. Acad. Sci. USA* **108**, 4822 (2011).
- ⁴⁰A. Altis, M. Otten, P. H. Nguyen, R. Hegger, and G. Stock, Construction of the free energy landscape of biomolecules via dihedral angle principal component analysis, *J. Chem. Phys.* **128**, 245102 (2008).
- ⁴¹R. Zwanzig, Diffusion in rough potentials, *Proc. Natl. Acad. Sci. (USA)* **85**, 2029 (1988).
- ⁴²J. C. F. Schulz, L. Schmidt, R. B. Best, J. Dzubiella, and R. R. Netz, Peptide chain dynamics in light and heavy water: Zooming in on internal friction, *J. Am. Chem. Soc.* **134**, 6273 (2012).
- ⁴³I. Echeverria, D. E. Makarov, and G. A. Papoian, Concerted dihedral rotations give rise to internal friction in unfolded proteins, *J. Am. Chem. Soc.* **136**, 8708 (2014).
- ⁴⁴D. Chandler, *Introduction to Modern Statistical Mechanics*, Oxford University, Oxford, 1987.
- ⁴⁵To obtain the correct free energy of state **4**, the trajectories are propagated until this state is left again.
- ⁴⁶D. Nagel and G. Stock, msmhelper: A Python package for Markov state modeling of protein dynamics, *J. Open Source Softw.* **8**, 5339 (2023).
- ⁴⁷D. Nagel, S. Sartore, and G. Stock, Toward a benchmark for Markov state models: The folding of HP35, *J. Phys. Chem. Lett.* **14**, 6956–6967 (2023).
- ⁴⁸N.-V. Buchete and G. Hummer, Coarse master equations for peptide folding dynamics, *J. Phys. Chem. B* **112**, 6057 (2008).
- ⁴⁹O. Lemke and B. G. Keller, Density-based cluster algorithms for the identification of core sets, *J. Chem. Phys.* **145**, 164104 (2016).
- ⁵⁰D. Nagel, A. Weber, B. Lickert, and G. Stock, Dynamical coring of Markov state models, *J. Chem. Phys.* **150**, 094111 (2019).
- ⁵¹A. Perez, F. Sittel, G. Stock, and K. Dill, Meld-path efficiently computes conformational transitions, including multiple and diverse paths, *J. Chem. Theory Comput.* **14**, 2109 (2018).
- ⁵²M. Biswas, B. Lickert, and G. Stock, Metadynamics enhanced Markov modeling: Protein dynamics from short trajectories, *J. Phys. Chem. B* **122**, 5508 (2018).
- ⁵³S. Mehdi, D. Wang, S. Pant, and P. Tiwary, Accelerating all-atom simulations and gaining mechanistic understanding of biophysical systems through state predictive information bottleneck, *J. Chem. Theory Comput.* **18**, 3231 (2022).
- ⁵⁴Note that we deliberately refer in Fig. 3 to the left-hand-side states by 'l' and 'L' and to the right-hand-side state by 'r' and 'R', although the common definition in the Ramachandran plot is the other way round.
- ⁵⁵D. van der Spoel, E. Lindahl, B. Hess, G. Groenhof, A. E. Mark, and H. J. C. Berendsen, Gromacs; fast, flexible and free, *J. Comput. Chem.* **26**, 1701 (2005).
- ⁵⁶W. F. van Gunsteren, S. R. Billeter, A. A. Eising, P. H. Hünenberger, P. Krüger, A. E. Mark, W. R. P. Scott, and I. G. Tironi, *Biomolecular Simulation: The GROMOS96 Manual and User Guide*, Vdf Hochschulverlag AG an der ETH Zürich, Zürich, 1996.
- ⁵⁷I. G. Tironi and W. F. van Gunsteren, A molecular dynamics simulation study of chloroform, *Mol. Phys.* **83**, 381 (1994).
- ⁵⁸L. Riccardi, P. H. Nguyen, and G. Stock, Free energy landscape of an RNA hairpin constructed via dihedral angle principal component analysis, *J. Phys. Chem. B* **113**, 16660 (2009).
- ⁵⁹S. J. Wodak et al., Allostery in its many disguises: From theory to applications, *Structure* **27**, 566 (2019).

Supplementary Material for:

Log-periodic oscillations as real-time signatures of hierarchical dynamics in proteins

Emanuel Dorbath,¹ Adnan Gulzar,¹ and Gerhard Stock¹

*Biomolecular Dynamics, Institute of Physics, Albert Ludwigs University,
79104 Freiburg, Germany^{a)}*

(Dated: 21 November 2023)

^{a)}Electronic mail: emanuel.dorbath@physik.uni-freiburg.de; stock@physik.uni-freiburg.de

I. THEORY AND METHODS

A. Timescale analysis

The time evolution of a observable $S(t)$ can be expressed by a sum of K exponential response functions

$$S(t) = s_0 - \sum_{k=1,K} s_k e^{-t/\hat{\tau}_k} \quad (1)$$

with the time scales $\hat{\tau}_k$ and amplitudes s_k . The term s_0 with $\hat{\tau}_0 \rightarrow \infty$ yields an offset.

In the presented analysis, the amplitudes in Eq. (1), the so-called spectrum, are obtained from a minimization fit. Here, the minimization tool `minimize` from `scipy.optimize`¹ is used with the default algorithm and a tolerance of 10^{-3} . This is a local minimization algorithm with a high dependency on the respective starting values, which therefore must be chosen carefully. Multiple combinations of starting parameters might be reviewed to find the most appropriate one. The expression to minimize is²

$$\chi^2 - \lambda_{\text{reg}} S_{\text{ent}} \quad (2)$$

with the entropy S_{ent} and the regularization parameter λ_{reg} . The χ^2 function is given as

$$\chi^2 = \sum_t^T \left(\hat{S}(t) - \sum_{k=0,K} s_k e^{-t/\hat{\tau}_k} \right)^2, \quad (3)$$

where the data trajectory is denoted as $\hat{S}(t)$, the number of trajectory frames as T and the number of fitting parameters as $M = K + 1$. Note, that for the analysis the trajectory frames are converted from the usual linear spacing into logarithmic spaced frames, which heavily reduces the number of frames used. The entropy in Eq. (2) is defined as

$$S_{\text{ent}} = \sum_{k=0,K} \left\{ \sqrt{s_k^2 + 4\tilde{s}^2} - 2\tilde{s} - s_k \log \left[\left(\sqrt{s_k^2 + 4\tilde{s}^2} + s_k \right) / 2\tilde{s} \right] \right\} \quad (4)$$

where the coefficient \tilde{s} is chosen as uniform element $\tilde{s} = (\hat{S}_{\text{max}} - \hat{S}_{\text{min}})/(100M)$, with the 'nonlinear enhancement factor' of $1/100$.²

The regularization parameter in Eq. (2) is an important quantity as it controls over- and underfitting and hence influences the obtained spectrum. As first step, a good regularization parameter λ_{reg} can be derived using two promising schemes:

- χ^2 -distribution:² For a random variable which is χ^2 -distributed it is expected, that the χ^2 -value is around the number of degrees of freedom $N_{\text{DOF}} = T - M$. To ensure this, λ_{reg} is increased until this is the case. However, with this scheme a too conservative estimation of λ_{reg} might be the result, i.e., λ_{reg} is too large and only the slowest of all time scales is resolved.

- Bayes criterion:³ For this strategy, the Bayesian posterior probability $P_0(\lambda_{\text{reg}}) \propto \lambda_{\text{reg}}^{N_{\text{DOF}}} e^{\lambda_{\text{reg}} S_{\text{ent}} - \chi^2}$ is used. The regularization parameter is chosen where the probability distribution has its maximum value. As the exponential expression is likely to result in divergences or is below numerical resolution, it is necessary to use the logarithm of $P_0 \rightarrow \ln P_0 = N_{\text{DOF}} \ln \lambda_{\text{reg}} - (\chi^2 - \lambda_{\text{reg}} S_{\text{ent}})$ and rescale the expression $\ln P_0 \rightarrow \ln P_0 / (\ln P_0^{\text{max}}/10)$. The rescaling enables a more strongly pronounced maximum. Finally, $\ln P_0$ is transformed back $\ln P_0 \rightarrow e^{\ln P_0}$ and normalized to its maximum.

The two methods are compared in Figure S1. Two drastically different values for λ_{reg} are obtained, where the χ^2 method is over a order of magnitude larger than the one of the Bayesian probability. It is seen that latter is a better choice, which gives access to faster time scales while the χ^2 one only resolves the slowest time scale.

We note that the number of time scales and their range should be chosen with care. Reducing the fit range can result in artifacts at the boundaries, which is more likely to happen for the fast times as there is also no dominating time scale in the vicinity. Furthermore, if $S(t)$ is monotonic increasing, we can restrict ourselves to $s_k \geq 0$, which may improve the fit.

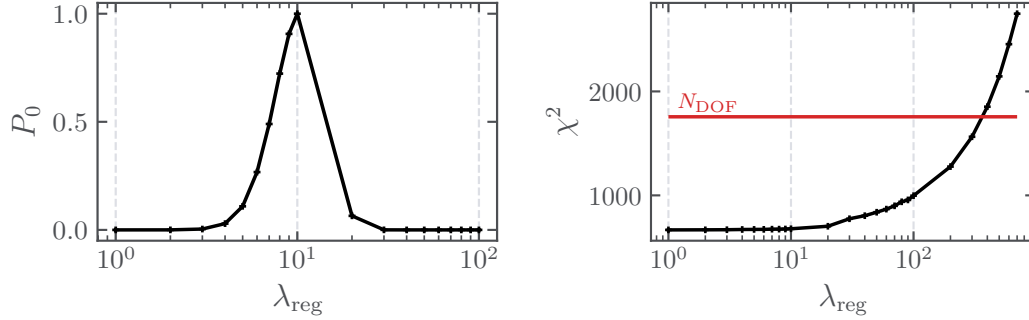


FIG. S1. Derivation of the optimal regularization parameter λ_{reg} used for the time scale analysis of the 1D model. In a) the Bayesian method and in b) the χ^2 -method is shown. The red line indicates the number of degrees of freedom N_{DOF} .

B. Log-periodic power law

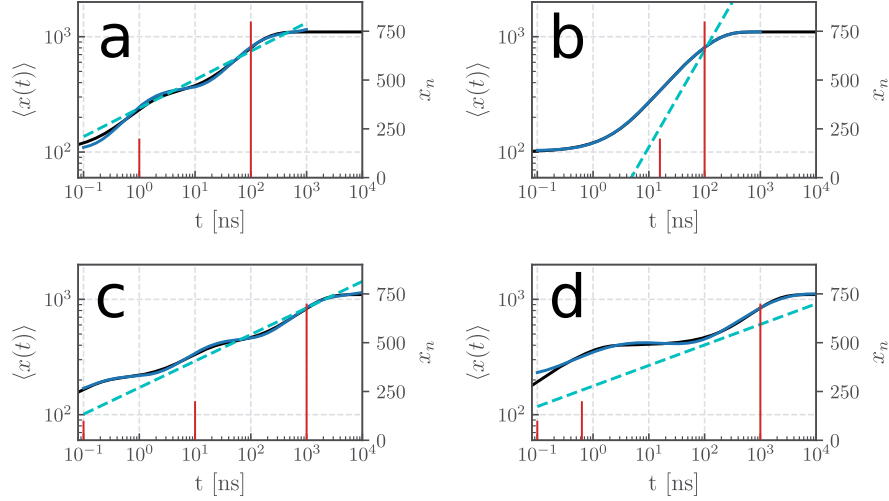


FIG. S2. Fit of a multiexponential model $S(t) = \sum_n s_n e^{-t/\tau_n}$ with only two (top) or three (bottom) main timescales τ_n and associated amplitudes s_n to the log-periodic power law $S(t) = s_a + s_b t^\alpha + s_c t^\alpha \cos(\frac{2\pi}{\tau_{\log}} \log t + \varphi)$. (a) Using two timescales that are more than one decade apart, i.e., $\log \tau_1 - \log \tau_2 \equiv \Delta_{12} = 2$, we obtain fits showing two well-defined log-oscillations with $\tau_{\log} \approx \Delta_{12}$. (b) If the timescales are too close to each other ($\Delta_{12} \lesssim 1$), we effectively see only a single exponential term without log-oscillations. (c) For three roughly logarithmically equidistant and well separated timescales, we obtain three well-defined log-oscillations. (d) If two of the timescales are too close to each other, we find only two exponential terms and two log-oscillations.

II. RESULTS FOR 1D MODEL

A. Simulations

The 3000 trajectories are generated via simulations of the Langevin equation at $T = 300$ K and a time step of $\delta t = 0.4$ ps.⁴ Each trajectory starts at $x = 0$ and are only stopped when x becomes ≥ 12.3 , i.e., the final energy barrier to **4** is crossed. This means there are not back transitions once state **4** is reached and only **1**→**4** are present. However, with this scheme each trajectory has its own individual length which makes the derivation of a averaged time trace problematic. We circumvent this problem by repeating the final frame of all trajectories to match with the longest one of ≈ 1.2 μ s. As we are interested in the time trace on a logarithmic time axis, we space each trajectory logarithmically such that in each decade approximately the same number of frames are present.

Fast fluctuations are reduced by Gaussian filtering, with a standard deviation of 2 frames for single trajectories and 6 frames for the averaged time trace. The latter is simply derived as arithmetic mean over the single trajectories x_i while the standard deviation of the mean is calculated as unbiased estimator

$$\sigma_{\bar{x}} = \frac{\sum_i^N |x_i - \bar{x}|^2}{N(N-1)} \quad (5)$$

where both x_i and \bar{x} are time dependent and N are the number of produced trajectories.

In Figure S3a, the average of the mean position $\langle x(t) \rangle$ for different numbers of trajectories is presented. The selected trajectories are smoothed after averaging as it is done for the actual analysis ($\sigma = 6$ frames on a logarithmic scale). For few trajectories $N < 10^2$ there are still significant and fast fluctuations visible, which might be misinterpreted as oscillations as seen in the respective log-log Figure S3b. These fluctuations vanish completely for $N > 10^3$.

B. Markov state model

The Markov state model is generated using a lag time of $\tau_{\text{lag}} = \delta t = 0.4$ ps. Each trajectory is transformed into state trajectories with the 4 states: **1** [-0.6,0.7], **2** [3.6,5.8], **3** [9.2,10.8] and **4** > 12.3 . Three implied time scales are obtained at $t_1 = 145$ ns, $t_2 = 1.3$ ns and $t_3 = 0.7$ ns which are constant over the whole time as seen in Figure S3c. By deriving the eigenvectors of the transition matrix, the flux between the respective states for each time scale can be seen, displayed in Figure S3e. The slowest one corresponds to the **1**→**4** while the second one is mostly the transition back into the initial state. The final and fastest time scale are transitions from state **1** and **3** into state **2**.

The validity of the Markov state model is verified by a Chapman-Kolmogorov test. For each of the 3 states, multiple lag times $k\tau_{\text{lag}}$ are used to derive the both sides of the equation

$$T(k\tau_{\text{lag}}) = T^k(\tau_{\text{lag}}). \quad (6)$$

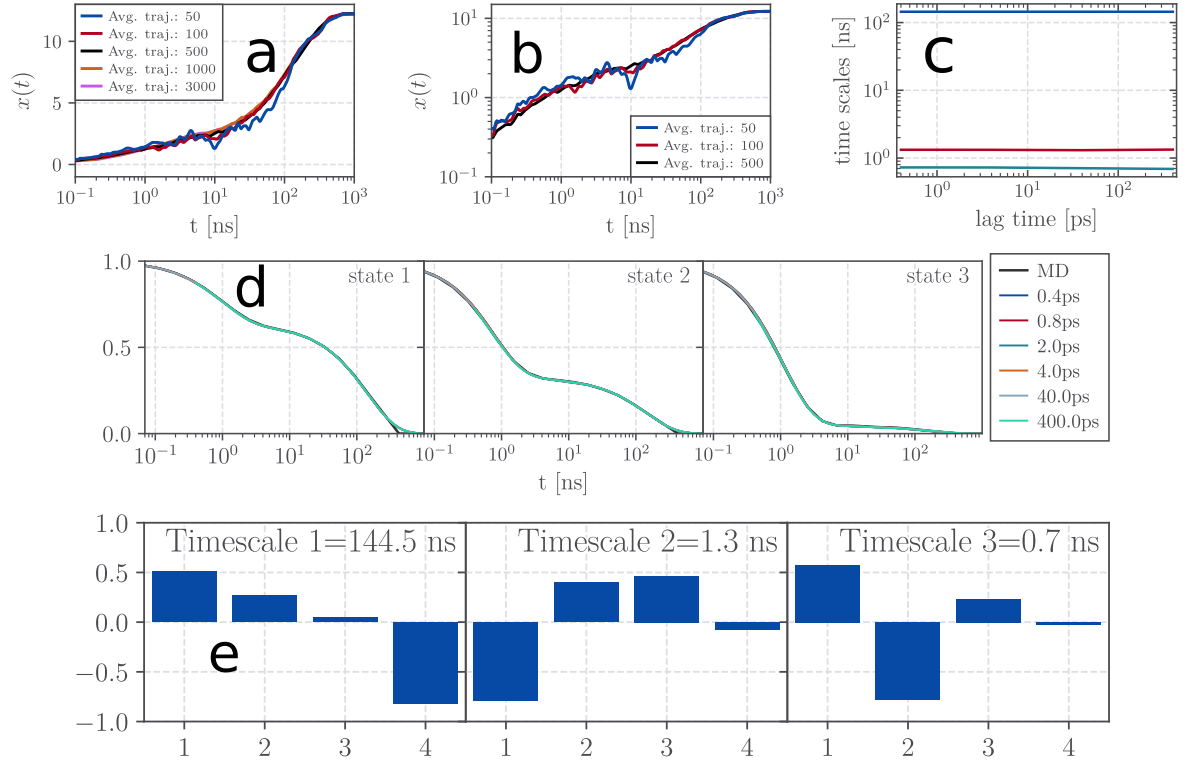


FIG. S3. (a) Mean position $\langle x(t) \rangle$ of the 1d model, using different numbers of trajectories. (b) double logarithmic representation of $\langle x(t) \rangle$. c) Implied time scales for various lag times. The time scales are almost constant over several orders of magnitude verifying a highly Markovian system. d) Chapman-Kolmogorov test for the 3 time scales and various lag times. Perfect Markovianity is verified for all lag times. e) Values of the eigenvectors of the transition matrix for the three implied time scales. The first time scale describes the forward propagation into state **4**, the second the backwards transition into state **1** and the third one a flux into state **2**.

The left hand side, referred to as MD, is the transition probability estimated for a lag time $k\tau_i$, while for the right hand side the transition probability for lag time τ_{lag} is propagated k times. Finally, a projection onto the diagonal elements is performed. As seen in Figure S3d, for both short and long lag times, a very good match with the MD is observed, verifying a high Markovianity.

C. Equilibrium autocorrelation function

The autocorrelation function is derived for a single $16 \mu\text{s}$ long equilibrium trajectory.⁴ An expected decay towards zero is seen which is reached latest at 100ns. A time scale analysis is performed for this correlation function giving rise to two time scales at 25 ns and 1.3 ns.

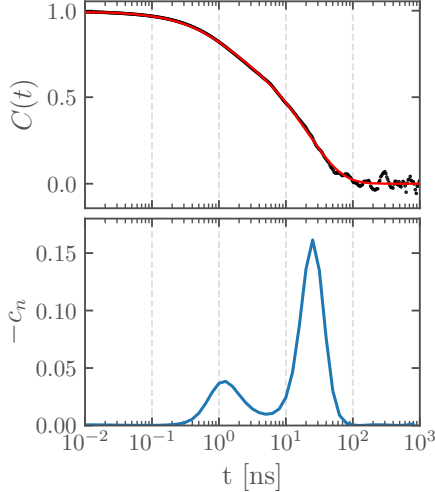


FIG. S4. Time scale analysis of the ACF for a single $16 \mu\text{s}$ long trajectory with $\lambda = 0.1$ and 50+1 fit parameters. In black the ACF is shown while in red the respective fit.

III. RESULTS FOR AIB₉

A. Trajectory slicing and data preparation

Initially, a $8 \times 2 \mu\text{s}$ long continuous equilibrium trajectory is generated with an effective time step of $\delta t = 1 \text{ ps}$. As stated in the main text, the quantity to describe Aib₉ best is the cumulative angle $\Phi = \sum_{i=3}^7 \phi_i$ over the 5 inner dihedral angles. We are interested in L→R transitions and thus, it is need to slice the EQ trajectory.

To this end, a Gaussian smoothing with $\sigma = 2 \text{ ps}$ is applied and the trajectory is transformed into a state trajectory with the two states L= $[-500^\circ, -200^\circ]$ and R= $[200^\circ, 500^\circ]$. All frames which do not match one of the states is set as undefined as they are irrelevant for the slicing procedure. Next, dynamical coring⁵ is applied with a coring time $t_{\text{cor}} = 100 \text{ ps}$, i.e., to be counted as L/R state the state trajectory must remain uninterrupted t_{cor} in the respective state. Finally, the trajectory is sliced from the respective first frame in L to the first one in R, thus giving the same data structure as for the 1D model. In total this gives 63 L→R transitions.

B. Markov state model

For the Markov State Model, the 6 states visible in Φ are used which are defined as $\pm 25^\circ$ around their theoretical core: L= -250° , rL= -150° , rrL= -50° , Rll= 50° , Rl= 150° and R= 250° . The 63 trajectories are again transformed into state trajectories, however now unmatched frames are set to the latest populated state. To enforce the L→R transition, the final frame is always set to be in R and repeated often enough to be not missed by the lag time.

An optimal lag time is derived at which the implied time scales become linear w.r.t. the lag rates. This is fulfilled at $\tau_{\text{lag}} = 0.5$ ns, see Figure S5a. In total 5 implied time scales are derived with the two most important ones being at $t_1 = 73.9$ ns and $t_2 = 2.7$ ns. With the eigenvectors of the transition matrix, the slower one describes the full conformational change L→R, while the next faster one is the result of transition of the central metastable states to the outer ones. All other time scales represent mixtures of various processes (Figure S5b).

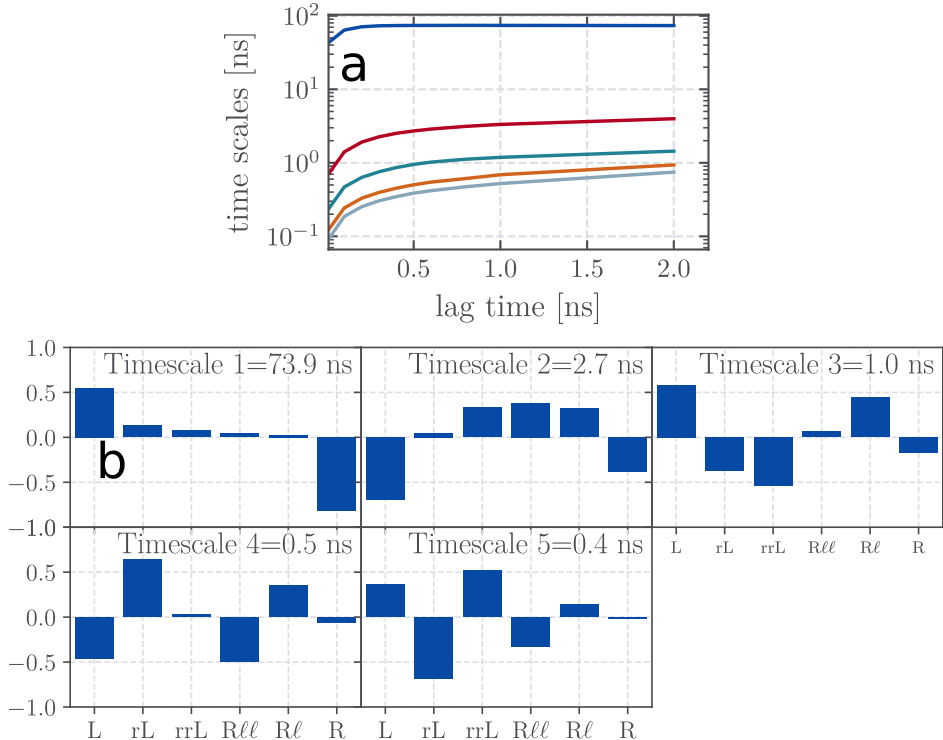


FIG. S5. a) Implied time scales for various lag times. The timescales become approximately constant at $\tau_{\text{lag}} = 0.5$ ns. b) Eigenvectors of the transition matrix.

REFERENCES

- ¹E. Jones et al., SciPy: Open source scientific tools for Python, 2001–2018.
- ²V. A. Lórenz-Fonfría and H. Kandori, Transformation of time-resolved spectra to lifetime-resolved spectra by maximum entropy inversion of the Laplace transform, *Appl. Spectrosc.* **60**, 407 (2006).
- ³V. A. Lórenz-Fonfría and H. Kandori, Practical aspects of the maximum entropy inversion of the laplace transform for the quantitative analysis of multi-exponential data, *Appl. Spectrosc.* **61**, 74 (2007).
- ⁴B. Lickert, S. Wolf, and G. Stock, Data-driven Langevin modeling of nonequilibrium processes, *J. Phys. Chem. B* **125**, 8125 (2021).
- ⁵D. Nagel, A. Weber, B. Lickert, and G. Stock, Dynamical coring of Markov state models, *J. Chem. Phys.* **150**, 094111 (2019).